Hindawi
IET Electrical Systems in Transportation
Volume 2023, Article ID 6635396, 14 pages
https://doi.org/10.1049/2023/6635396

Research Article

Operation and Control of an Active Power Collector for Roadside Feeding Electric Road System

Saleh A. Ali,[1] **Volker Pickert**,[1] **Mohammed A. Alharbi**,[2] **Handong Li**,[3] **and Haris Patsios**[1]

[1]*School of Engineering, Newcastle University, Newcastle upon Tyne NE1 7RU, UK*
[2]*Faculty of Engineering, Taibah University, 42353, Medina, Saudi Arabia*
[3]*Department of Mathematics, Physics and Electrical Engineering, Northumbria University, Newcastle upon Tyne NE1 8ST, UK*

Correspondence should be addressed to Saleh A. Ali; saleh.ali@newcastle.ac.uk

Received 24 June 2023; Revised 25 August 2023; Accepted 11 September 2023; Published 26 October 2023

Academic Editor: Natarajan Prabaharan

The integration of electric vehicles (EVs) as an environmentally sustainable alternative to traditional fossil fuel cars faces a range of technological obstacles, including battery technology, charging infrastructure, and standardization. Dynamic conductive road charging (DCRC) of EVs at high speed has the potential to overcome the technical limitations of existing static charging methods. An intelligent motorway system for EVs called tracked electric vehicle (TEV) was proposed to incorporate the latest technologies of dynamic road charging, autonomous driving, and smart city data into transport infrastructure. This paper presents the operation and control of an active bipolar power collection unit (PCU) for the TEV system. The PCU is seamlessly integrated within the wheel structure of an EV using the concept of a stationary-hub wheel, enabling conductive power transfer from roadside conduction rails while the vehicle is in motion. The PCU is equipped with various features designed to maintain the contact force (CF) with the conduction rails, effectively handle instances of wheel bouncing and vibrations, and ensure a consistently smooth dynamic power transfer. This paper presents the experimental validations of the active PCU controls, including the operation sequence of the PCU, CF control, and PCU interaction with wheel bouncing.

1. Introduction

About a quarter of global greenhouse gas (GHG) emissions arise from road transportation. Electric vehicles (EVs) have emerged as a potential resolution for establishing sustainable practices within road travel [1]. Nevertheless, several technological hurdles obstruct the broad implementation of EVs: battery technology, charging infrastructure, and standardization. The current constraints in battery technology encompass elements like a restricted electric driving range, extended charging duration, and an uncertain battery lifespan [2]. Furthermore, owing to the battery's lower specific energy compared to gasoline or diesel, a substantial battery pack is required to attain an acceptable driving range, consequently augmenting the vehicle's weight and cost [2, 3]. Quick charging entails various challenges, including implications for battery systems regarding heat management and constraints, as well as ramifications for the distribution power system in relation to phase imbalances, harmonic infusions, and the coordination of protection systems [4]. The lack of consistent standards and the interoperability of charging systems is another market impediment to the growth of the EV market.

Extensive research endeavors are currently focused on enhancing the energy density of EV batteries and optimizing the charging efficiency of stationary fast chargers. However, interstate traveling at high speeds quickly depletes a vehicle's battery, limiting the driving range [4]. Introducing dynamic conductive road charging (DCRC) at elevated driving speeds has the capability to expedite the acceptance of EVs as a sustainable alternative to traditional fuel-based vehicles [5, 6].

A smart, efficient highway concept referred to as tracked electric vehicle (TEV) system was recently proposed [7]. TEV system can accommodate an enormous number of EVs that can be charged while driving at high speeds. TEV track is a single, narrow, electrically powered, and enclosed lane, so overtaking is not possible, and weather disruption does not affect the system operation [7]. In the TEV system, EVs travel autonomously in platoons at high speeds of

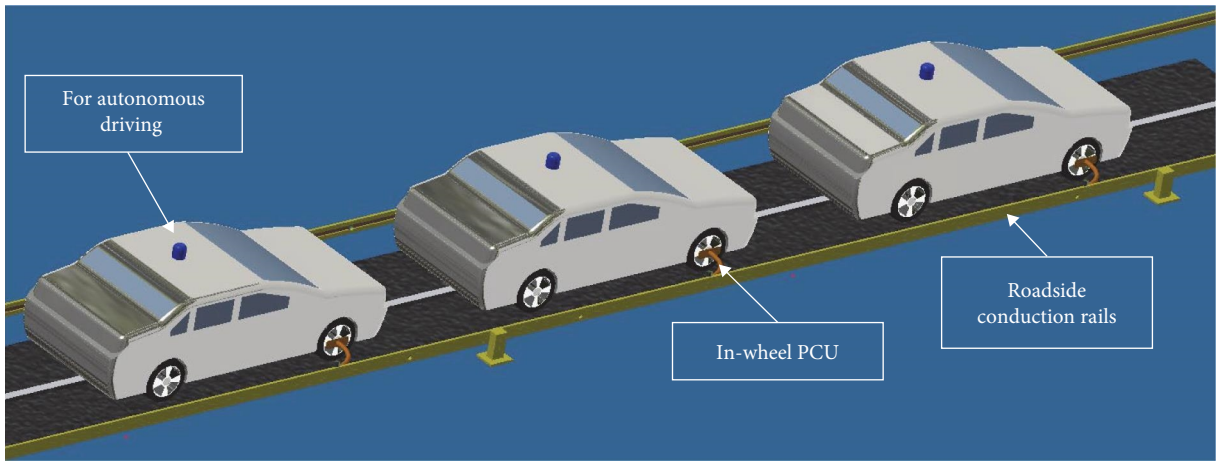

Figure 1: EVs drive autonomously in a platoon in the TEV system.

200 km/hr and small intervehicle distances, as shown in Figure 1. Driving in convoys with close intervehicle spacings is a technique that reduces overall aerodynamic drag and hence increases overall system efficiency [8]. Therefore, the TEV system can be an efficient dynamic charging platform for EVs to avoid the limitations of available charging systems.

The Siemens e-Highway showcases a dynamic charging system designed for freight transportation. This setup involves utilizing two parallel top-mounted pantographs to acquire power from two overhead power lines. Notably, the pantographs are equipped with spacious collector shoes in relation to the width of the lines, allowing them to slide laterally within a broad range without necessitating precise shoe alignment beneath the lines. When no overhead line is detected, the pantographs retract automatically, and the vehicle transitions to diesel hybrid power. Siemens' technology draws inspiration from well-established trolleybus and railway systems. However, it is important to note that this solution may not be viable for passenger EVs [9].

Honda conducted tests on a DCRC system. The EV power collection unit (PCU) is equipped with a 1.5-m long arm housing two rolling contacts referred to as "twin roller," which can effectively transmit up to 450 kW of power at speeds reaching 150 km/hr. The extension and retraction of the power collection arm to the EV's chassis are managed through an electric linear actuator. The arrangement includes a bipolar power track that carries a voltage of 750 V DC and is integrated within the crash barrier. Furthermore, this system operates on the basis of a substantial stationary battery storage system capable of supplying substantial power to the in-motion vehicle. This setup offers the advantage of providing a 3-km rapid charging lane for every 52 km travel distance [10, 11].

The ground-charging PCUs are referred to as "pickups." Three different pickup technologies based on ground charging have already been demonstrated for dynamic ground charging: Alstom Aesthetic Power Supply (APS), Elways, and ElonRoad [5, 12]. The Alstom APS presents a 750-V DC rail system wherein power tracks are seamlessly integrated into the road surface. While initially designed for trams, this technology can be customized for EVs. The collection device, referred to as the pickup shoe, is a bipolar PCU equipped with automated and precise lateral positioning capabilities [13]. ElonRoad concept is based on 1-m segments mounted on the road's surface. This approach incorporates a 1.5-m long pickup mechanism featuring three sliding contacts operating at 600 V DC. The leading connector establishes contact just before the trailing connector loses connection [14]. The Elways approach is identical to the other two systems, with two significant differences: the road surface is embedded with two 10-cm deep parallel slots, and the track operates on a single-phase 50 Hz power supply. The Elways technology involves a precise active positioning mechanism installed beneath the car's chassis to connect the pickup to the electrified slot [15].

In general, none of the existing approaches has been demonstrated at a continuous driving speed exceeding 100 km/hr, except for the Honda system, which underwent testing at speeds of 150 km/hr. However, it operated within an intermittent charging mode, featuring a 3-km charging lane for every 52 km traveled. Consequently, these solutions do not align with the TEV system. Moreover, all the presently available DCRC systems necessitate significant modifications to EVs. This entails either redesigning and reinforcing the EV roof or the development of chassis to accommodate PCUs. Thus, these technologies prove impractical due to their associated high costs.

The authors have proposed a unique concept in the domain of DCRC called the "wheel-hub active PCU for TEV system" described in [16]. This study successfully demonstrated a pioneering DCRC concept in which an active PCU was affixed to a stationary-hub wheel to enable the conductive power transfer from roadside conduction rails during vehicle motion. This innovative approach was motivated by several factors: (1) The distinct characteristics of the TEV system, wherein the track is a singular narrow lane, and the EVs drive autonomously without overtaking, resulting in uninterrupted power conduction and a reduction in undesirable discontinuous conduction transients; (2) The utilization of the stationary-hub wheel concept, influenced by Orbis

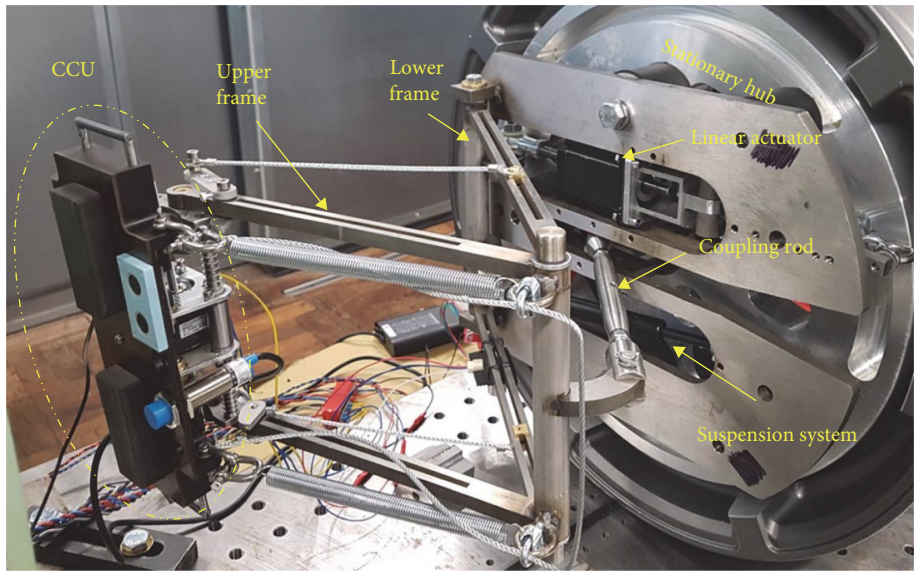

Figure 2: Proposed stationary-hub wheel PCU [16].

Ring-Wheel technology, employing an eccentric wheel drive motor to establish a static hub, consequently reducing the torque needed for wheel propulsion by 40% and elevating braking efficiency by 30% [17]; (3) The incorporation of an in-wheel active suspension system, which effectively reduces wheel vibration and, thereby, improves the quality of power transfer via the wheel-hub PCU.

The prototype wheel-hub PCU represents a hybrid configuration, functioning as a bipolar minipantograph that effectively gathers power from the roadside conduction rails. This design is inspired by the combination of high-speed trains with third-rail charging systems. It operates as an active PCU, efficiently maintaining the desired contact force (CF) between the sliding contacts and the conduction rails. Additionally, the system is outfitted with dual linear stepper actuators and a suspension mechanism for extending, retracting, and accommodating horizontal and vertical wheel vibrations or deflections.

While the design and experimental validation of the wheel-hub PCU for this concept are extensively covered in [16], this article primarily aims to introduce the PCU's control scheme and operation sequence. The paper is structured as follows: Section 2 introduces the structure of the wheel-hub PCU, Section 3 describes the operation of the PCU, Section 4 elaborates on the control strategy, Section 5 presents the findings of the experimental validation, and, finally, Section 6 provides a concise summary that encapsulates the entire content of the paper.

2. Structure of the Wheel-Hub PCU

The wheel-hub PCU is composed of four main parts: current collection unit (CCU), kinematic mechanism, linear actuator, and suspension system. The PCU is analogous to the pantograph in railway applications in terms of the articulating frames, actuation, and suspension system. However, there are key differences between the head of the pantograph and the CCU of the PCU. Figure 2 shows the proposed PCU mounted on a static-hub wheel.

The CCU is a bipolar unit with two wide carbon strips with regard to the width of the conduction rails. This design allows the strips to move laterally across a wide range, eliminating the necessity for precise vertical alignment. The CCU can be appropriately referred to as a "smart CCU" for the following reasons: (1) It incorporates a load cell to monitor the CF between the carbon strips and conduction rails, and it regulates the desired CF through a primary linear actuator situated at the base of the PCU; (2) An inductive proximity sensor is integrated to detect the conduction rails, enabling the CCU to establish contact or retract to its home position as needed; (3) A linear actuator is integrated, enabling active movement upward and downward. This facilitates tasks such as scanning the conduction rails, interacting with wheel bouncing, and ensuring even wear distribution of the brushes; (4) It is provided with two ultrasonic distance sensors to monitor the horizontal and vertical positions of the CCU; and (5) The CCU is equipped with a three-axis vibration sensor and an infrared temperature sensor to monitor the vibration and temperature of the contact surface. The components of the CCU are shown in Figure 3 and described in detail below.

2.1. Sliding Contacts. The two sliding contacts are metallized carbon strips with a low coefficient of friction and a 10 A/cm^2 current density. The metallized carbon was made and provided by Morgan Advanced Materials, a major supplier to the railway and tramway industries around the world. The carbon brushes measure 8 cm by 3 cm and are strategically designed to be 5 cm broader than the conduction rails.

2.2. Brush Carrier. It measures 24 cm long by 7 cm wide and is made of Tufnol 1P/13 material, which is characterized by its low weight, high stiffness and hardness, and excellent electrical and thermal insulation.

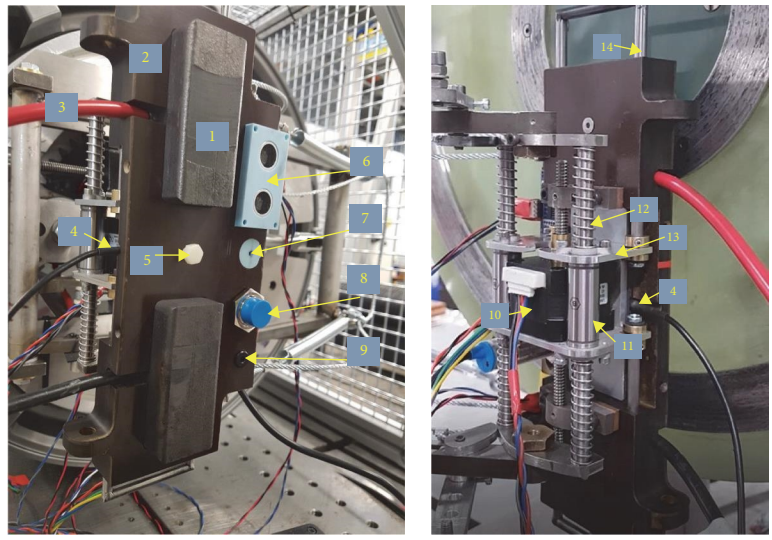

(a) (b)

FIGURE 3: The CCU [16]: (a) front view; (b) back view.

2.3. Power Cables. Two trirated 10 mm^2 red and black PVC cables, commonly known as BS6231 cables, are connected to the CCU brushes to transfer power to the resistor load.

2.4. Load Cell. A button load cell with a range of 50 kg (500 N) is used with an electrical signal output of 1 mV/V. The electrical output from the load cell is amplified, filtered, and measured using a strain gauge amplifier shield coupled with an amplifier AD8426.

2.5. Force Adjustor. An M6 flat-head screw is used for fine-tuning the CF offset between the carbon brushes and conduction rings.

2.6. Ultrasonic Distance Sensor (HC-SR04). The ultrasonic ranging module offers a noncontact measuring range of 2–400 cm with a ranging precision of up to 3 mm. The basic work principle is that the trig pin of the HC-SR04 transmits an ultrasound at 40 kHz through the air. When an object or obstacle reflects the high-frequency pulse, the sensor's echo pin receives it, and the ultrasonic transducer calculates the round-trip duration of the sound. The distance can be determined by halving the round-trip travel time and the sound speed (340 m/s) [18].

2.7. Vibration Sensor (ADXL335 Triple Axis). It is a three-axis acceleration measurement device with a full sensing range of ±3 g, where 1 g equals 9.8 m/s^2. The output signals are analog voltages that correspond to the acceleration magnitude. The deflection of the structure is measured using a differential capacitor. Acceleration deflects a moving mass and unbalances the differential capacitor, producing a sensor output with amplitude and direction proportional to the acceleration, *X*-, *Y*-, and *Z*-axes [19].

2.8. Inductive Proximity Sensor. It generates a magnetic field around the detecting surface using a coil and oscillator. When a metallic object enters the operating region of the sensor, an induction current is generated in the target object, Faraday's law, which creates a magnetic field that opposes the sensor's coil magnetic field, Lenz's law. The sensor's trigger circuit oversees the amplitude of the magnetic field oscillation, which triggers a change in the output state when it dips below a predefined threshold. The sensor's detection range varies based on the detected metal type. For instance, ferrous metals like iron can extend the detection range to 10 mm [20].

2.9. Infrared (IR) Temperature Sensor (MLX90614). This sensor contains an integrated IR-sensitive thermopile detector chip and signals conditioning circuitry. The thermopile is composed of thermocouple pairs connected in series. The measured output voltage is directly proportional to the temperature differential across a thermal resistance layer and the thermocouple junctions. It is factory calibrated for a large temperature range from 70 to 380°C, with high precision of 0.5°C throughout this range [21].

2.10. Stepper Linear Actuator (NEMA17). This stepper motor is a hybrid design that combines attributes of both permanent magnet and variable reluctance motors, resulting in superior step resolution, speed, and torque capabilities. The stepper motor is one of the most commonly used motors in motion control applications, especially in positioning applications, because it can be precisely controlled down to fractions of a degree without using feedback devices such as encoders or resolvers.

2.11. Linear Bearing. Two precise LM8UU-sized linear ball bearings are used to connect the CCU to the articulating mechanism, enabling the CCU to move freely upward and downward throughout its range of motion.

2.12. Pivotal Connector. This mechanism comprises a two-rod pivoting link, four compression springs with a stiffness of 0.50 N/m, and two linear bearings on both sides. It links the pressing plate of the CCU to the top of the end point of the upper frame.

2.13. Pressing Plate. The plate is a U-shaped aluminum plate with a thickness of 3 mm, designed to accommodate the linear bearings and connected to two sliding loops. It houses the integrated linear actuator and transmits the force the active suspension system applies to the brush carrier, achieving the desired CF.

2.14. Slider Loops. The CCU is equipped with two slider U-loops attached to the pressing plate and passing through the brush carrier, enabling it to slide upward and downward freely.

3. Operation of the PCU

The PCU is equipped with two stepper linear actuators, the primary and auxiliary actuators, which allow for active movement in both horizontal and vertical directions. The primary actuator, denoted as "Stepper1," is positioned at the base of the PCU frame. This actuator is responsible for extending and retracting the PCU horizontally and maintaining control over the CF between the sliding contacts and the power conduction rails. The CCU incorporates an auxiliary linear actuator known as "Stepper2," which is responsible for the vertical movement of the carbon brushes. This facilitates tasks such as identifying the conduction rails through a process, referred to as "scanning," ensuring even friction distribution across the brush surface, known as "swinging," and engaging with vertical wheel bouncing to maintain consistent power transmission, referred to as "bouncing." These linear actuators are managed by digital multistepping drive units (DM542T). All controllers are programmed using the C language on Arduino Uno microcontrollers, connected through a multichannel optocoupler module (PCF817) to enable sequential communication. Figure 4 shows a schematic depiction of the PCU's control architecture. The operational sequence of the PCU and complete program scripts for the control codes of Stepper1, Stepper2, and the monitoring system are shown in *Supplementary 1* and *Supplementary 2*.

4. Control of the PCU

The PCU controls include the operation sequence, CF regulation, scanning, swinging, and bouncing. This article presents experimental results for all these control functionalities. However, particular emphasis is given to presenting the modeling and simulation of the CF control, as it forms the primary objective of this active PCU.

4.1. Mathematical Modeling of the PCU. Kinematic and lumped mass models were employed to analyze the behavior of the PCU. The kinematic model was utilized to estimate the lengths and angles of the PCU frames in [16]. The modeling methodology described in this article involves the utilization of the lumped mass model to develop a controller responsible for the regulation of CF exerted by the PCU carbon strips on the conduction rails [22].

The lumped-mass model is an effective method for describing the PCU's physical features. For example, high-speed trains' pantographs consist of three interconnected masses: the head and upper and lower frames. It interacts with the mass of the overhead catenary, which has varying stiffness, creating a system with various natural frequencies. Consequently, it is regarded as a three degree of freedom (DOF) model [16, 23]. Nevertheless, the proposed PCU has been characterized as a single DOF system due to the following considerations: (1) The mass of the PCU is significantly smaller than that of a pantograph, and its interconnected frames hold nearly equivalent masses; (2) In contrast to overhead lines, the conduction rails have incredibly high, and time-invariant stiffness and their mass does not influence the behavior of the PCU [24]; thus, the interaction between the conduction rails and the PCU is minimal. Moreover, autonomous driving technology is assumed to effectively maintain the EV's position relative to the conduction rails [16]. Therefore, the PCU can be described as a parallel arrangement consisting of a mass-spring-damper system in conjunction with a linear actuator. This configuration is employed to uphold the desired CF by either injecting or dissipating energy through the suspension mechanism, as shown in Figure 5. This approach is analogous to the concept of active suspension technology [16, 25].

The PCU's dynamic motion equations can be expressed using Newton's second law as follows [16, 26]:

$$\Sigma F = ma, \tag{1}$$

$$mX_1'' = -b(X_1' - X_3') - k(X_1 - X_3) + F_a, \tag{2}$$

where m is the PCU's mass, k and b are the stiffness and damping of the suspension, respectively, X_1 and X_3 are the horizontal displacement, X_1', X_3' are the PCU speed and wheel vibration, respectively, F_a is the linear actuator force, and F_c is the CF.

State variables can be described as horizontal motion using the state–space representation:

$$x_1 = X_1, x_2 = \dot{x_1} = \dot{X_1}, x_3 = X_2 \text{ and } x_4 = \dot{x_3} = \dot{X_2}, \tag{3}$$

where x_1 and x_2 are the displacement and speed of the PCU, respectively, whereas x_3 and x_4 are the movement and vibration of the wheel, respectively.

Therefore, Equation (2) can be arranged in state–space form as follows:

$$\dot{x_2} = -\frac{k}{m}x_1 - \frac{b}{m}x_2 + \frac{k}{m}x_3 + \frac{b}{m}x_4 + \frac{F_a}{m} + F_d, \tag{4}$$

where F_d represents any external disturbance force.

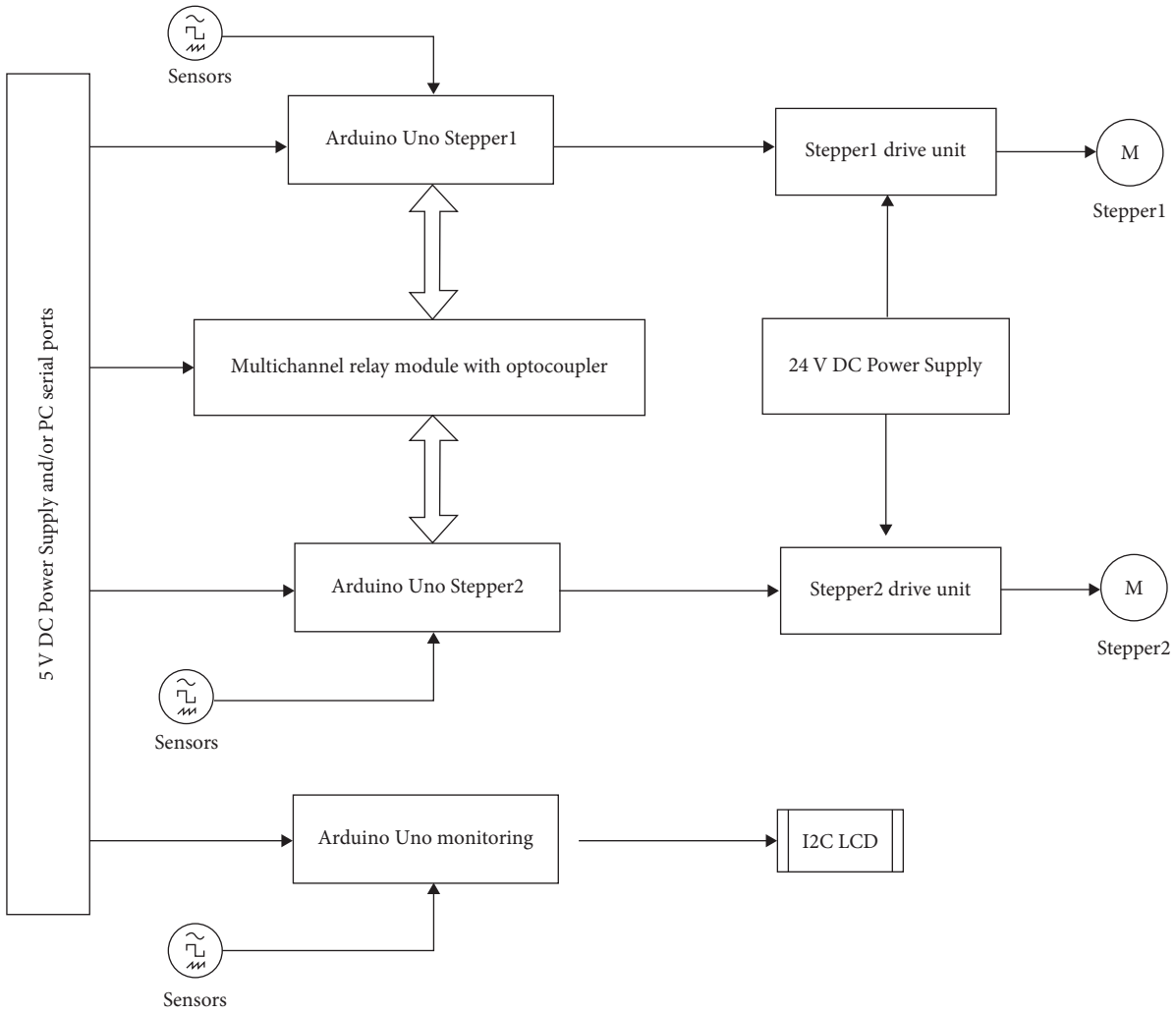

Figure 4: Control panel schematic diagram.

The general state–space representation form is given as follows [16, 26]:

$$\begin{aligned} \dot{x} &= Ax + Bu, \\ y &= Cx + Du, \end{aligned} \tag{5}$$

where A, B, C and D are the state space, input, output, and direct transmission matrices, respectively, x is the state variables, u is the system input, and y is the system output.

Thus, the state–space representation of the system is given as follows:

$$\begin{bmatrix} \dot{x_1} \\ \dot{x_2} \\ \dot{x_3} \\ \dot{x_4} \end{bmatrix} = \begin{bmatrix} 0 & 1 & 0 & 0 \\ -\dfrac{k}{m} & -\dfrac{b}{m} & \dfrac{k}{m} & +\dfrac{b}{m} \\ 0 & 0 & 0 & 1 \\ 0 & 0 & 0 & 0 \end{bmatrix} \begin{bmatrix} x_1 \\ x_2 \\ x_3 \\ x_4 \end{bmatrix} + \begin{bmatrix} 0 \\ \dfrac{1}{m} \\ 0 \\ 0 \end{bmatrix} F_a + \begin{bmatrix} 0 \\ 1 \\ 0 \\ 0 \end{bmatrix} F_d, \tag{6}$$

$$y = \begin{bmatrix} 1 & 0 & -1 & 0 \end{bmatrix} \begin{bmatrix} x_1 \\ x_2 \\ x_3 \\ x_4 \end{bmatrix}, \tag{7}$$

$$F_c = k(x_1 - x_3), \tag{8}$$

where y is the measured displacement.

4.2. Design and Simulation of CF Controller. The control strategy for regulating the CF draws inspiration from active suspension system technology. In contrast to the pantographs of high-speed trains, the CF control exclusively considers PCU parameters. Various techniques have been applied to govern the active suspension, including the utilization of mechanical impedance simulation [25], higher-order sliding mode control (HOSMC), integral sliding mode control (ISMC), proportional integral derivative (PID), and linear quadratic regulator (LQR) [27]. The PID

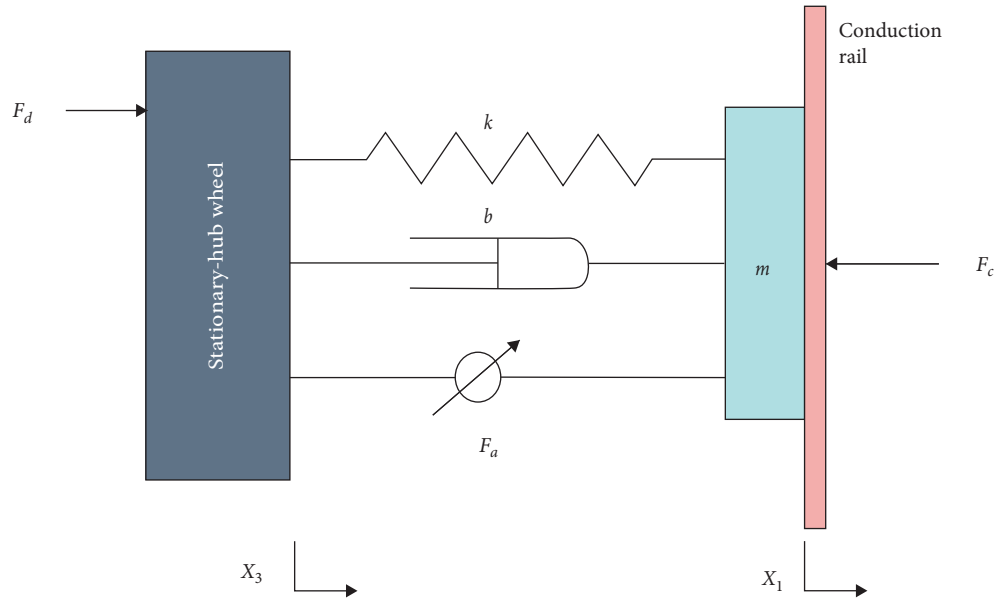

FIGURE 5: Lumped-mass model of the PCU.

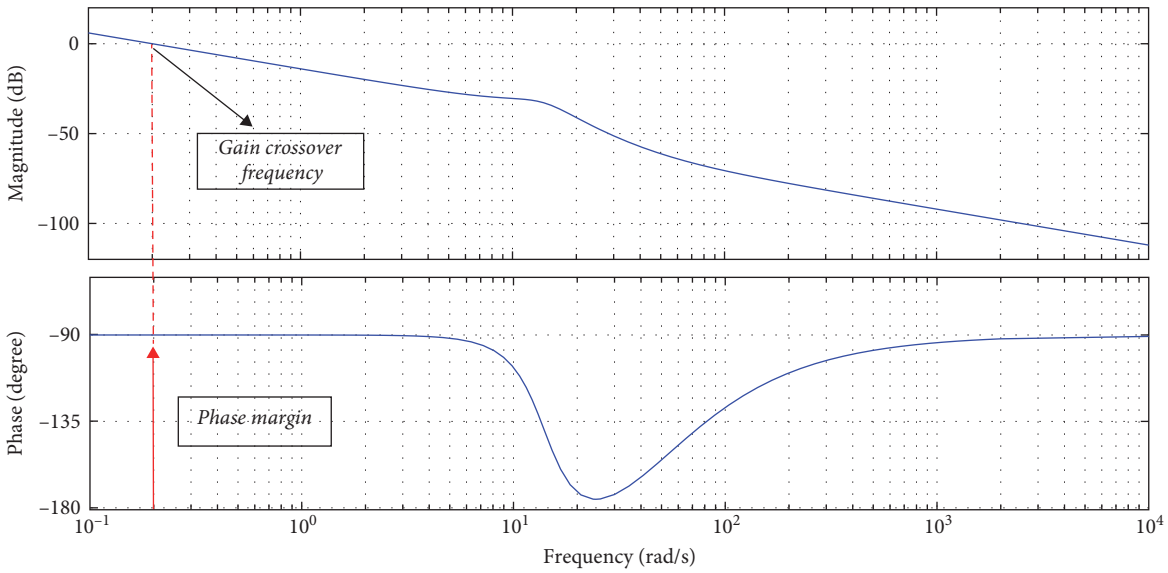

FIGURE 6: Bode diagram for the closed-loop system.

controller was used to regulate the CF for lab validation of the proposed approach.

A Simulink model was developed using the state–space representation of the PCU motion, as shown in Equations (5)–(7). The system parameters are: the mass of the PCU (m) = 5 kg; the suspension stiffness (K) = 1,000 N/m; the suspension damping (b) = 50 N m/s; and the force of the actuator (Fa) = 100 N. The CF was controlled using a PID controller. A graphical user interface (GUI) tool referred to as single-input-single-output (SISO) tool was utilized for PID controller design. When the transfer function's poles, zeros, or gain are modified, the SISO tool approach modifies the root locus and Bode graphs in real time. The PID Tuner software optimizes the robustness and performance of the plant's PID controller by adjusting the gains automatically. The PID tuning method with a first-order derivative filter is chosen to improve the controller's performance by adjusting the loop bandwidth and phase margin in the Bode plot. Figure 6 illustrates the Bode plot for the system's transfer function, offering insights into its stability, gain margin (GM), and phase margin (PM). GM and PM are quantified in decibels (dB) and degrees. Modifying GM and PM allows for control over the system's stability. Higher GM and PM values result in improved system stability [28]. Figure 6 shows the Bode diagram for the closed-loop system that demonstrates that the PM is +90° and GM is infinity since there is no phase

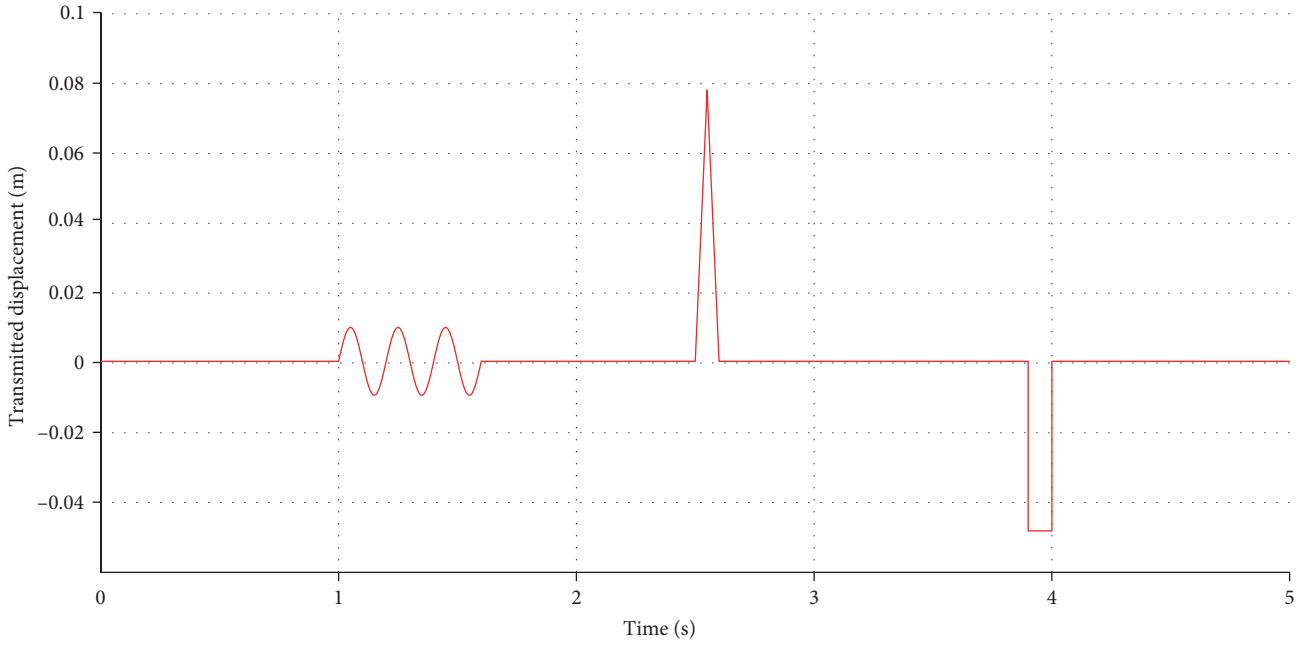

Figure 7: Disturbance signals.

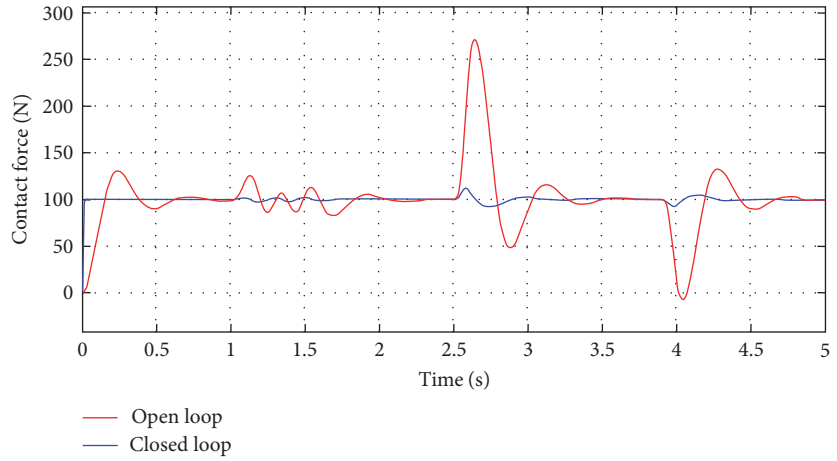

Figure 8: CF control simulation.

crossover frequency; therefore, the system is stable. The PID controller gains were exported to the Matlab workplace when the desired response was achieved, $Kp = 10$, $Ki = 200$, $Kd = 0.125$, $Tf = 0.001$, and then these gains were entered into the Simulink model establishing the closed-loop control system.

The system response to the step input of the desired CF (100 N) and the three different disturbance signals, as shown in Figure 7, are examined in open and closed control loops. This analysis is conducted to demonstrate the robustness of the PID controller that has been designed.

Figure 8 demonstrates the system response to the disturbance signals. The response to step input force is in the period 0–1 s. Characteristics of the open-loop system are 0.14 s rise time, 0.24 peak time, 0.8 s settling time, and 30% overshoot. The system's robust response with the PID controller has no overshoot, zero steady-state error, and a rise time of 0.01 s, resulting in a 14-fold performance enhancement over the open-loop system. The sinusoidal disturbance signal of 0.01 m amplitude and a frequency of 5 Hz, $F_d = 0.01\cos(10\pi t)$, $1\,\text{s} \le t \le 1.6\,\text{s}$, simulates an excessive vibration disturbance. The PID controller displays lowered and more controlled variation in the CF of around 5 N ripple with the same frequency as the vibration signal. In contrast, the response of the open-loop system is a distorted waveform with an average force ripple of 30 N. The random disturbance signals represent two different transient disturbance signals: a spike signal of 80 N at 2.5 s and a pulse signal of −50 N at 3.9 s. The closed-loop response exhibits robust performance, with less than 10% overshoot/undershoot, 0.5 s settling time, and zero steady-state error. On the other hand, the open-loop system response results in greater than 100%

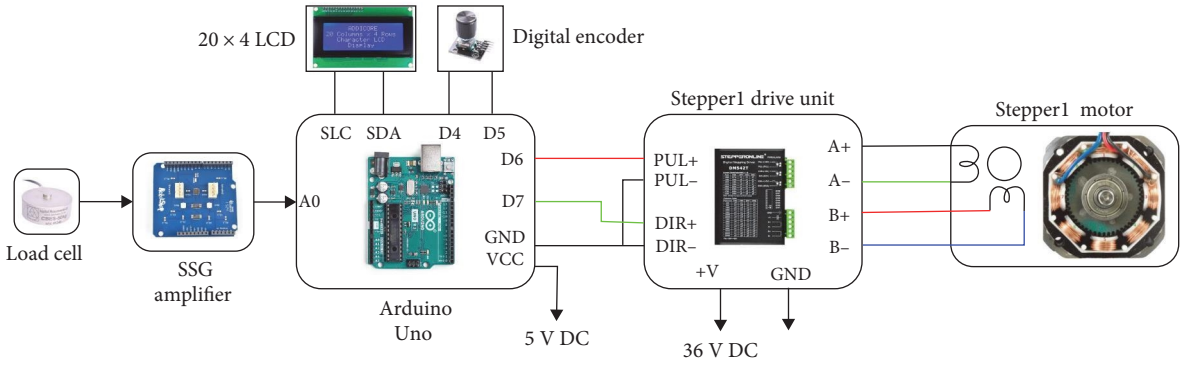

Figure 9: CF control loop.

overshoot and longer settling time, demonstrating the robustness of the designed PID controller.

5. Experimental Validation

An experimental platform was developed in-house to demonstrate the DCRC concept using the proposed active PCU mounted on a stationary-hub wheel along with a rotary power disk. The power disk has two conduction rings to simulate the TEV's conduction rails, which would be installed in the crash barrier [16]. This paper's practical testing scope is confined to motion and control assessments of the prototype PCU. The PCU is controlled by two stepper linear actuators, referred to as "Stepper1" and "Stepper2." The Stepper1 is controlled by a load cell to maintain the desired CF. In contrast, the Stepper2 is controlled using various controllers to perform different tasks: (1) To detect the conduction rings using an inductive proximity sensor, this process is referred to as "*scanning*"; (2) To distribute the wear uniformly across the carbon brushes employing a sequence controller, this function is known as "*swinging*"; and (3) To interact with the wheel bouncing utilizing an ultrasonic distance sensor, denoted as "*bouncing*."

5.1. CF Control. A load cell integrated into the CCU is linked to pin A0 of the Arduino Uno board. This setup enables the load cell to detect the CF as analog input through a Wheatstone amplifier shield, as shown in Figure 9. When CF deviates from the set point, the microcontroller sends pulse and direction output signals (D6 and D7) to the Stepper1 drive unit to correct this deviation. An adaptive PID controller is used to determine the response signal characteristics with two sets of parameters (Kp, Ki, Kd). The magnitude of the error determines the choice between these parameter sets. Conservative parameters ($Kp2 = 0.5$, $Ki2 = 0.075$, $Kd2 = 0.000025$) are used when the error is less than 10 N; otherwise, the controller calls for the aggressive set of parameters ($Kp1 = 1.5$, $Ki1 = 0.15$, $Kd1 = 0.000005$).

To replicate CF fluctuations, the CF set point was intentionally adjusted to different levels during the operation. This manipulation introduced control errors between the measured CF and the set point. The subsequent evaluation was conducted to assess the performance of the developed controller in handling these conditions. Figure 10 demonstrates how the force controller adjusts the actual CF in response to changes in the reference CF. During the operation of the power disk at a speed of 1,000 rpm, the CF set point was intentionally varied across different levels using commands from the Arduino serial monitor online data acquisition of the CF.

Figure 10 demonstrates the CF controller's rapid response to the ramping of the reference signal with an overshoot of less than 10% and CF ripples of around ±5 N. The variation in the CF is due to the extremely low sensitivity of the load cell (1 mV/V) and the narrow range of the measured force compared with the entire range of the load cell. The expected measured CF range is only around 100 N or about one-fifth of the entire range of the load cell (500 N). According to the load cell calibration with the SGS amplifier, the full range of the load cell (500 N) represents 1,024 while the 0 offset value is 340, using the Arduino Uno's ADC resolution (10 bits). Consequently, the ADC raw value of the full range of the load cell is 1,024–340 = 684, whereas the raw value of the maximum measured CF is only 684/5 = 137. The resolution of the ADC in mV/bit is 5,000/1,024 = 4.88 mV/bit; hence, the full detected force range in mV is only $137 \times 4.88 = 0.669$ V, which is a relatively narrow sensitivity measuring range. Furthermore, the vibration of the spinning power disk or any other manufacturing defect in the PCU's frames could cause these ripples.

5.2. Scanning and Swinging Control. Scanning and swinging controllers employ nearly identical code to drive the Stepper2, prompting it to raise and lower the carbon brush carrier. However, these controllers differ in their sequence orders, intended goals, and the distinct operational conditions they address.

The scanning process involves a single-cycle operation initiated by the Stepper1 controller when the CCU reaches the designated scanning level. This cycle entails moving the brush carrier from the center position to the upper limit, then to the lower limit, and finally returning to the center position. This process terminates when a proximity sensor detects one of the conduction rings, prompting the brushes to return to the center position and the Stepper1 controller to shift the CCU to the tracking position. When none of the conduction rings is detected, the scanning cycle is completed, interrupting the PCU operating sequence.

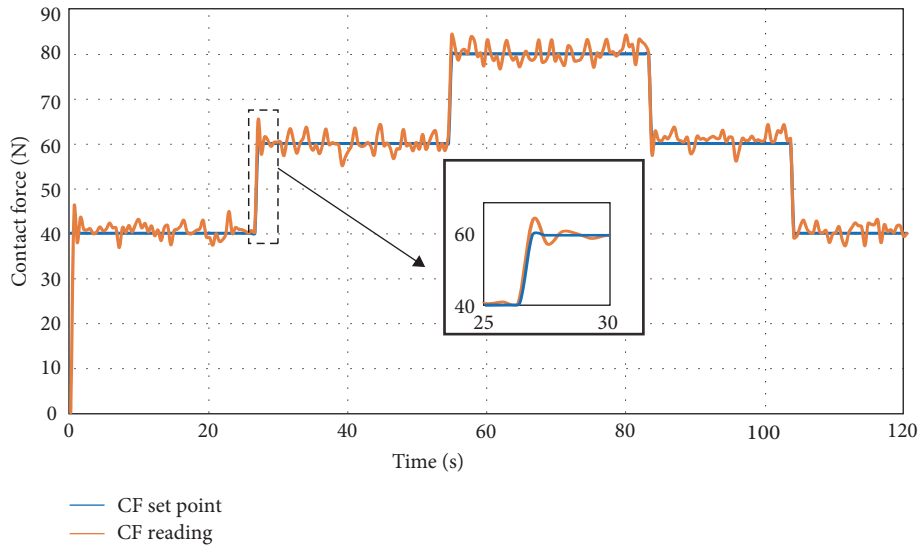

Figure 10: CF controller tracking varying reference value.

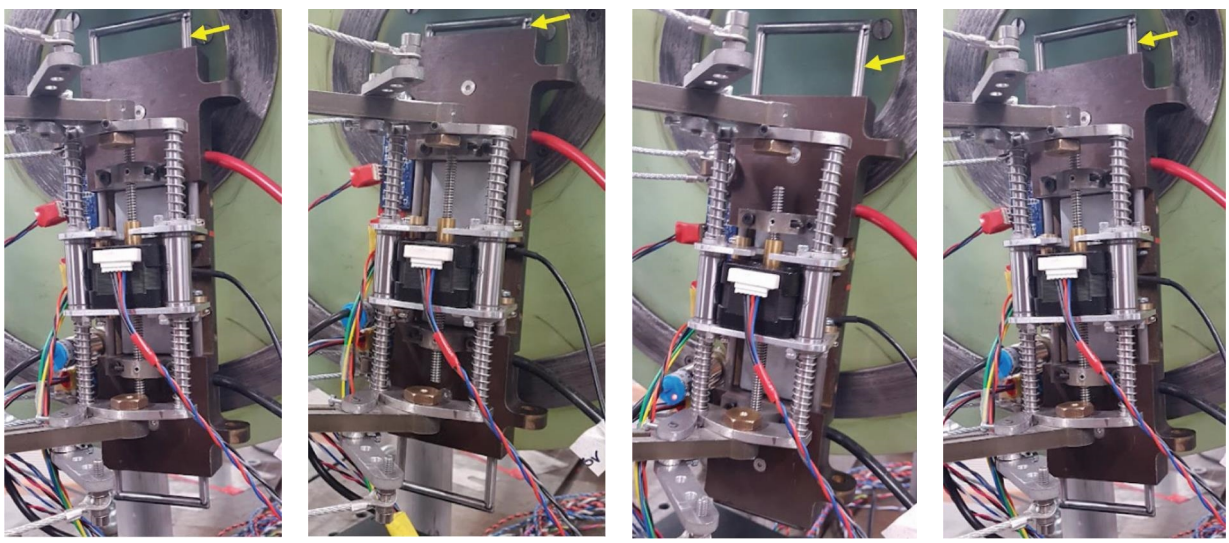

Figure 11: One cycle of the CCU motion: (a) at the center position; (b) at the upper end; (c) at the lower end; (d) back to the home position.

Swinging is a multicycle operation initiated by the CF controller when the CCU operates under steady speed and full load conditions. This operation ceases as the CCU starts to retract toward the home position. During the swinging procedure, the Stepper2 mechanism coordinates the oscillation of the brush carrier through an up-and-down motion, performed at a relatively moderate speed. This motion is intended to equally distribute friction wear throughout the surface of the sliding contacts. This can be seen as analogous to the zigzagged overhead lines used in high-speed railway applications. Figure 11 shows one complete operation cycle of the CCU's motion, as indicated by the yellow arrows.

The oscilloscope image, as shown in Figure 12, presents the direction and stepping signals of the drive units of the two steppers, indicating the timing of communication between them. Magenta pulses and green direction signals represent the Stepper1 drive signals, whereas the Stepper2 drive signals are in dark blue pulses and light blue direction signals.

The numbering scheme, as shown in Figure 12, corresponds to the order of the operational sequence of the two steppers: (1) Stepper1 is extending the PCU to the scanning level; (2) Stepper2 began scanning in the low direction and was inverted to high when the conduction rings were detected; (3) Stepper1 is moving the PCU to the tracking level; (4) Stepper2 is swinging for two cycles indicated by the direction signal change; and (5) Stepper1 is retracting the PCU to the home position indicated by the direction signal change. Furthermore, the figure demonstrates that the scanning cycle was terminated when the proximity

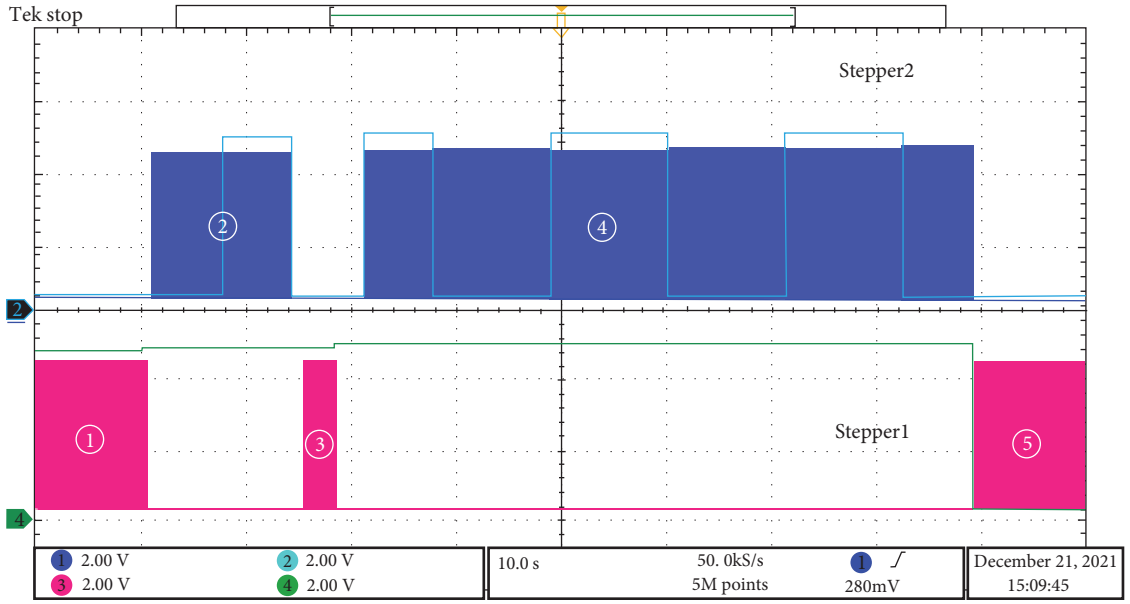

Figure 12: The operation sequence of the PCU.

sensor detected a conduction ring, whereas the swinging process lasted two complete cycles and ended when Stepper1 retracted the PCU.

5.3. Bouncing Control of the Brush Carrier. The PCU incorporates three functionalities to address wheel bounce: two mechanical approaches and one electrical control method. The initial wheel deflection, within a range of up to 2.5 cm, is effectively handled through the utilization of two linear bearings and four compression springs situated along the sliding connection that establishes the linkage between the CCU and the upper frame of the PCU. When the wheel deflection exceeds the 2.5 cm threshold, an ultrasonic distance sensor affixed to the PCU is triggered, prompting the activation of the Stepper2 mechanism to initiate a counteracting motion in the opposite direction. This corrective action aims to address deflections within the 2.5–5 cm range; in cases where the wheel bounce surpasses the 5 cm threshold, an additional movement of 2.5 cm upward or downward becomes achievable because the carbon brushes are 5 cm wider than the conduction rails. As a result, the PCU is effectively equipped to accommodate a total wheel bounce distance of up to 7.5 cm in both upward and downward directions. This capability is attributed to the broader reach of the carbon brushes beyond the width of the conduction rails. This section addresses the control loop of Stepper2, which includes an ultrasonic distance measurement sensor attached to the lower frame of the PCU facing the road surface to monitor the ground clearance of the PCU. Road surface disturbance was emulated by placing a flat object 13 cm beneath the ultrasonic distance sensor, as shown in Figure 13.

As the flat object is elevated, the measured distance experiences a decrease, mimicking a scenario where the vehicle encounters a pothole. This reduction in measured distance triggers the bouncing controller. Given that the measured distance falls below the predefined set point, the

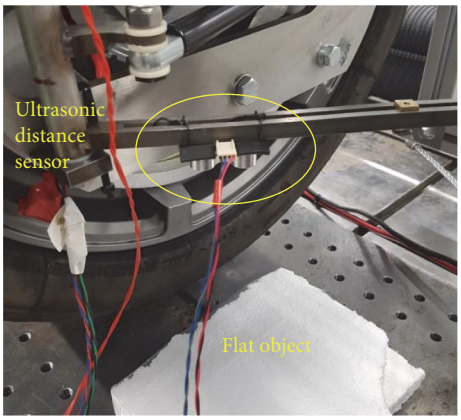

Figure 13: Wheel bouncing emulation.

controller computes the rotation direction (low) required to elevate the carbon brush carrier. The magnitude of movement and the controller's response are influenced by the disparity in distance (error) and the parameters of the PID controller. Upon the removal of the flat object, the measured distance experiences a sudden increase from low to high, exceeding the reference distance. In response, the rotation direction is switched to high to correct this error and prevent any disruption in power transfer; this simulates the wheel bouncing upward. As the flat object is repositioned back in its original position, the controller then commands the carbon brush carrier to return to the center position. Figure 14 visually represents the scenarios outlined above through numbered cases 1–3. In these cases, the microcontroller's direction pin status is marked as low for upward movement in cases 1 and 3 and high for downward movement in case 2. Moreover, the figure illustrates that the pulse clusters in case 2 are broader than those in cases 1 and 3. This distinction in pulse width arises because the motions in the latter cases

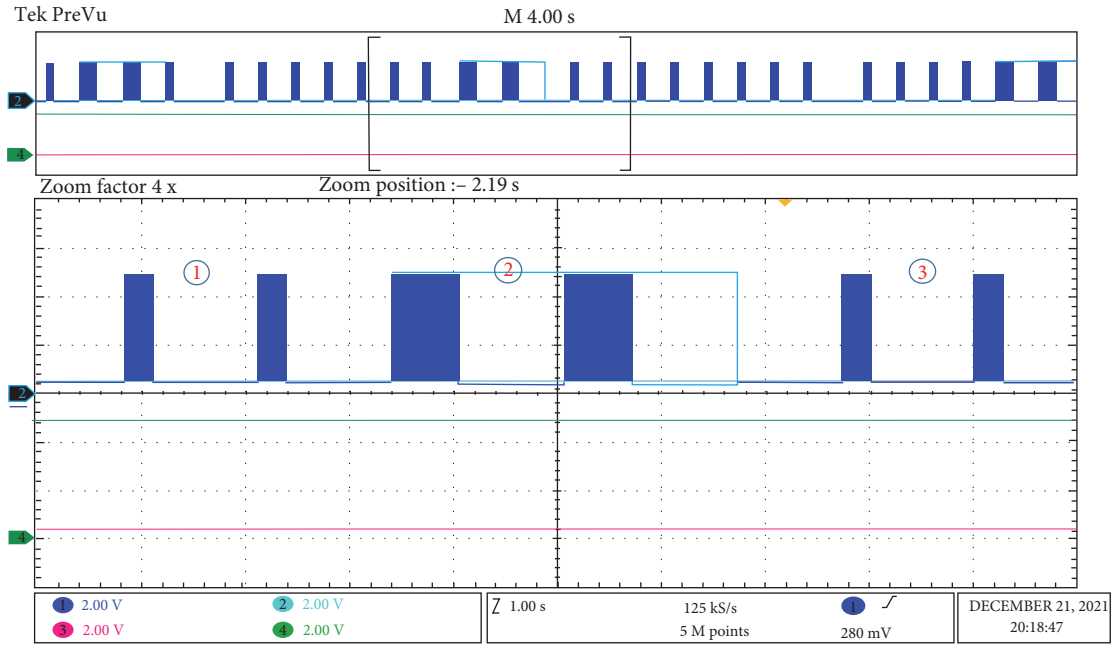

Figure 14: Bouncing controller output direction and pulses to the Stepper2 drive unit.

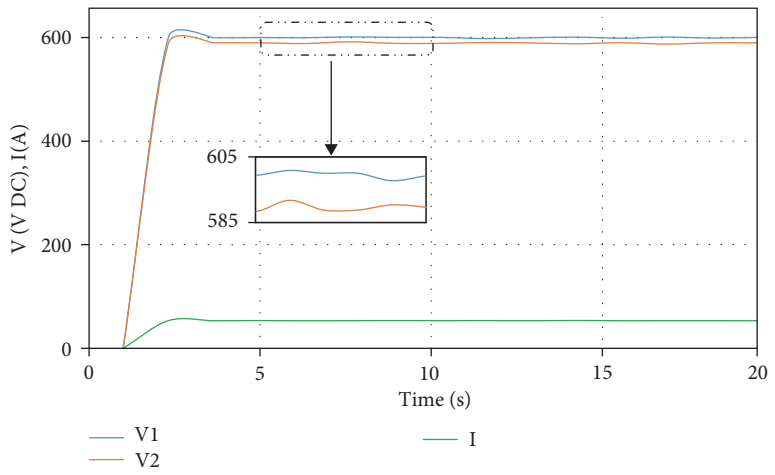

Figure 15: Oscilloscope exported readings of V1, V2, and I [16].

involve transitions from/to the zero position, whereas the motion in case 2 entails a shift from a lower distance to a higher distance. This leads to a higher proportional gain, thus influencing the width of the pulse bunches.

5.4. Dynamic Conductive Power Transfer. The validation of the DCRC concept at high speed was achieved by transmitting 30 kW of power from the rotating power disk while it was spinning at 2,400 rpm and powered by a 600-V DC source to resistive load through the wheel-hub PCU. The effectiveness of transferring power through dynamic conduction was tested at varying loads (15 and 30 kW) and speeds (500, 1,000, and 1,500 rpm) before reaching the intended speed of 2,400 rpm, equivalent to a velocity of 200 km/hr [16]. Figure 15 demonstrates the successful dynamic power transfer at full load and the target speed (2,400 rpm) [16]. The illustrated values represent the input and output voltages of the spinning power disk, denoted as V1 and V2. The voltage levels are 600 V for V1 and 590 V for V2. The current flowing through the rotating conduction rings is indicated as I and amounts to 50 A when operating under a full load [16]. The presence of electrical contacts between the carbon brushes and the rotating conduction rings generates a voltage difference of 10 V, attributed to the resistance within these contacts. This discrepancy in voltage is accompanied by a corresponding power loss, which is maintained within acceptable thresholds for this particular application (10% tolerance). This is particularly important as this application typically involves electrical arcing during the conduction process [29, 30].

6. Conclusion

This paper presents the operation and control of a prototype active PCU. The proposed PCU was employed to empirically verify a new concept of roadside DCRC. The bipolar active PCU was devised and mounted on a stationary-hub wheel to collect the power from spinning conduction rings, which emulate the roadside conduction rails. The PCU was fitted with a range of mechanical and control attributes that allow it to detect the conductor rails during start-up and maintain the desired CF during operation by actively reacting to the wheel bouncing and deflection. A mathematical model for the PCU was developed and used to design and simulate the CF controller. The PCU operation sequence, CF control, and other control features, including scanning, swinging, and bouncing capabilities, were experimentally validated. DCRC tests were successfully conducted at a rotational speed of 2,400 rpm, equivalent to 200 km/hr, and a full load of 30 kW. The simulation and experimental results are introduced and discussed in this article.

Data Availability

The operation sequence of the power collector and software data used to support the findings of this study are included within the supplementary information file(s).

Conflicts of Interest

The authors declare that they have no conflicts of interest.

Acknowledgments

This research was funded by Tracked Electric Vehicle (TEV Project), Philadelphia Scientific Ltd.

Supplementary Materials

Supplementary 1. Operation sequence of the PCU.

Supplementary 2. Control codes for Stepper1, Stepper2, and monitoring system.

References

[1] International Energy Agency, IEN, "CO2 emissions from fuel combustion—highlights," , p. 165, 2019.

[2] G. Haddadian, M. Khodayar, and M. Shahidehpour, "Accelerating the global adoption of electric vehicles: barriers and drivers," *The Electricity Journal*, vol. 28, no. 10, pp. 53–68, 2015.

[3] "Adoption of electric vehicles: which factors are really important?" 2021 https://www.tandfonline.com/doi/epub/10.1080/15568318.2020.1818330?needAccess=true.

[4] R. Collin, Y. Miao, A. Yokochi, P. Enjeti, and A. von Jouanne, "Advanced electric vehicle fast-charging technologies," *Energies*, vol. 12, no. 10, Article ID 1839, 2019.

[5] J. Suul and G. Guidi, "Technology for dynamic on-road power transfer to electric vehicles," *SINTEF Energy Research*, 2018, https://www.sintef.no/globalassets/project/elingo/18-0733-rapport-3-technology-for-dynamic-on-road-6-til-nett.pdf.

[6] M. Adhikari, L. P. Ghimire, Y. Kim, P. Aryal, and S. B. Khadka, "Identification and analysis of barriers against electric vehicle use," *Sustainability*, vol. 12, no. 12, Article ID 4850, 2020.

[7] W. Jones, "Tracked electric vehicles (TEV) system, TEV Project," 2022, https://tevproject.com/#booklet.

[8] S. Ali, V. Pickert, and H. Patsios, "Grid demand reduction for high-speed dynamic road charging by narrowing inter-vehicle distance," in *2018 IEEE International Conference on Electrical Systems for Aircraft, Railway, Ship Propulsion and Road Vehicles & International Transportation Electrification Conference (ESARS-ITEC)*, pp. 1–6, IEEE, Nottingham, 2018.

[9] D. Bateman, D. Leal, S. Reeves et al., "Electric road systems: a solution for the future," *TRL Academy*, vol. PPR875, 2018.

[10] T. Tajima, H. Tanaka, T. Fukuda et al., "Study of high power dynamic charging system'," in *WCX^{TM} 17: SAE World Congress Experience*, 2017.

[11] T. Tajima, "450-kW conductive electric road system by Honda," p. 5, 2020.

[12] M. Alakula and F. J. Marquez-Fernandez, "Dynamic charging solutions in Sweden: an overview," in *2017 IEEE Transportation Electrification Conference and Expo, Asia-Pacific (ITEC Asia-Pacific)*, pp. 1–6, IEEE, Harbin, China, 2017.

[13] P. Veyrunes, P. Duprat, and J.-L. Hourtane, "Ground-level feeding systems from rail to road," in *2017 IEEE Transportation Electrification Conference and Expo, Asia-Pacific (ITEC Asia-Pacific)*, pp. 1–4, IEEE, Harbin, China, 2017.

[14] D. Zethraeus, "Elonroad auto charge every where," *Elonroad*, 2019, https://elonroad.com/wp-content/uploads/2019/11/Elonroad_intro2.pdf.

[15] G. Asplund and B. Rehman, "Conductive feeding of electric vehicles from the road while driving," in *2014 4th International Electric Drives Production Conference (EDPC)*, pp. 1–9, 2014.

[16] S. A. Ali, V. Pickert, M. A. Alharbi, H. Li, and H. Patsios, "Wheel hub active power collection unit for dynamic conductive road charging," *IEEE Transactions on Transportation Electrification*, vol. 9, no. 1, pp. 1927–1936, 2023.

[17] Technology, "Orbis® Making Mobility Green," July 2020, https://orbisdriven.com/our-technology/.

[18] P. Bradt and D. Bradt, *Science and Engineering Projects Using the Arduino and Raspberry Pi: Explore STEM Concepts with Microcomputers*, Springer, Berkeley, CA, 2020.

[19] "ADXL335.pdf," September 2021, https://www.analog.com/media/en/technical-documentation/data-sheets/ADXL335.pdf.

[20] "3-Wire inductive proximity sensor | how to read the datasheet | RealPars. PLC programming courses for beginners | RealPars, 2020," September 2021, https://realpars.com/proximity-sensor-datasheet/.

[21] "MLX90614-Datasheet-Melexis-953298.pdf," September 2021, https://www.mouser.co.uk/datasheet/2/734/MLX90614-Datasheet-Melexis-953298.pdf.

[22] Y. Song, H. Ouyang, Z. Liu, G. Mei, H. Wang, and X. Lu, "Active control of contact force for high-speed railway pantograph-catenary based on multi-body pantograph model," *Mechanism and Machine Theory*, vol. 115, pp. 35–59, 2017.

[23] P. Yu, K.-Z. Liu, M. Yokoyama, and M. Wu, "Robust control of contact force for pantograph-catenary System'," in *2018 57th Annual Conference of the Society of Instrument and Control Engineers of Japan (SICE)*, pp. 713–718, IEEE, Nara, 2018.

[24] M. Paudel, L. J. Lim, F. F. Yap, and K. Kho, "Vibration analysis of the third rail structure of a mass rapid transit system with structural defects," *Applied Sciences*, vol. 11, no. 18, Article ID 8410, 2021.

[25] B. Allotta, L. Pugi, and F. Bartolini, "An active suspension system for railway pantographs: the T2006," *Proceedings of the Institution of Mechanical Engineers Part F: Journal of Rail and Rapid Transit*, vol. 223, no. 1, pp. 15–29, 2009.

[26] J. Zhang, H. Zhang, B. Song, S. Xie, and Z. Liu, "A new active control strategy for pantograph in high-speed electrified railways based on multi-objective robust control," *IEEE Access*, vol. 7, pp. 173719–173730, 2019.

[27] Y. Shahid and M. Wei, "Comparative analysis of different model-based controllers using active vehicle suspension system," *Algorithms*, vol. 13, no. 1, Article ID 10, 2020.

[28] N. Sayyaf and M. S. Tavazoei, "Desirably adjusting gain margin, phase margin, and corresponding crossover frequencies based on frequency data," *IEEE Transactions on Industrial Informatics*, vol. 13, no. 5, pp. 2311–2321, 2017.

[29] A. Reyes, "IEEE recommended practice for monitoring electric power quality, IEEE Std 1159-2009 (revision of IEEE Std 1159-1995)," pp. 1–94, 2009.

[30] A. D. Femine, D. Gallo, D. Giordano, C. Landi, M. Luiso, and D. Signorino, "Power quality assessment in railway traction supply systems," *IEEE Transactions on Instrumentation and Measurement*, vol. 69, no. 5, pp. 2355–2366, 2020.